Radiative Emission in Incident Air Shocks from 3-7 km/s

Brett A. Cruden[1]
AMA Inc at NASA Ames Research Center, Moffett Field, CA, 94035, USA

Augustin Tibere-Inglesse[2]
NASA Postdoctoral Fellow at NASA Ames Research Center, Mountain View, CA, 94035, USA

This paper reports experimental characterization of shock layer radiation in Air at low velocities (3-7 km/s) measured in the Electric Arc Shock Tube at NASA Ames Research Center. This included shock conditions from 3-5 km/s and 2-10 Torr to measure ultraviolet and mid-infrared radiation from NO and two nominal equilibrium conditions of 6 km/s, 2.0 Torr and 7 km/s, 1.4 Torr which were intended to produce 1 bar post-shock conditions and produced atomic N and O radiation along with the UV NO bands. The 10 Torr, 4 km/s has a 2.2 bar post-shock pressure and the mid-infrared measurement is in good agreement with equilibrium. The ultraviolet and visible ranges however show radiation in excess of equilibrium. Photorecombination and spin-splitting are shown to have significant impact on the spectrum, however there are also appears to be an overpopulation of the NO(A) state. The 4 km/s, 2.25 Torr condition is investigated as a reacting flow, and post-shock temperature and number density profiles are extracted. Finally, the 6 and 7 km/s conditions are shown to be in good agreement with similar measurements at the Oxford T6 facility but the radiation is again in excess of equilibrium.

I. Introduction

Extensive testing in the NASA Ames Electric Arc Shock Tube (EAST) has been conducted in the last 15 years to quantify radiation in hypersonic air relevant to Earth vehicle re-entry conditions [1-7]. These tests have mostly focused on Lunar return conditions with velocities in excess of 10 km/s [8]. The lowest velocity studied throughout these tests was at 7 km/s, where radiation of NO was significant in the ultraviolet [5]. Additionally, one test series in pure N_2 was conducted at velocities as low as 6 km/s, where radiation from molecular N_2 was detected [9, 10]. There is currently significant interest in the scientific community for understanding shock layer kinetics, including thermal non-equilibrium effects, at velocities lower than this bound, between 3-6 km/s [11-13]. Because radiation is still observed at 6 km/s, it is anticipated that quantitative emission spectroscopy diagnostics may continue to be employed in this lower velocity regime. There has been additional interest in better understanding the early stages of air ionization in hypersonic flight from 5-9 km/s [14]. A test series was therefore conducted in EAST to probe the NO formation at 3-5 km/s and reproduce equilibrium air data obtained in other facilities from 6-7 km/s. This paper reports emission spectroscopy measurements in the test series. Concurrent laser absorption spectroscopy measurements have been reported in [15].

Ultraviolet emission spectroscopy was recently performed in the CalTech Hypervelocity Expansion Tube (HET) [16]. Measurements were made by stagnating an expanding flow on a test article at an enthalpy and density equivalent to a 4 km/s, 2.4 Torr incident shock. Data was presented in relative units and analyzed for temperature. There have been some attempts to model this flow using Direct Simulation Monte Carlo (DSMC) method [17]. Similar measurements have also recently been performed in the Sandia Hypersonic Shock Tunnel (HST) [18]. While UV NO radiation originates from electronically excited states of NO, vibrational transitions from the electronic ground state are

[1] Senior Research Scientist, Aerothermodynamics Branch, and AIAA Associate Fellow
[2] NASA.Postdoctoral Fellow, Aerothermodynamics Branch

expected in the mid-infrared near 5.2 μm and have also been the subject of recent modeling studies [19]. We are not aware of any recent attempts to measure these features in similar facilities, although this is possible in the EAST facility using the same equipment previously employed to detect CO and CO_2 radiation for Martian entries [20, 21]. This paper reports new measurements of NO infrared and ultraviolet radiation in this regime, from 3-5 km/s. Comparisons to some of the infrared data reported in the present paper have already been presented in the literature [22].

The measurement of equilibrium air radiation in a plasma torch at atmospheric pressure with temperature from 6000-7500K has been previously reported and the resulting air radiation models are hence thought to be well validated [23-25]. The Oxford T6 facility has recently attempted to produce these equilibrium test conditions by using velocities and fill pressures that would produce a 1 bar post-shock condition and so could be compared to the plasma torch measurements and models [26]. The results showed a significant underprediction of the radiance, due in large part to background continuum radiation. As similar results have been observed in the lower range of previous EAST tests [3], it is desired to also reproduce these conditions in the EAST facility.

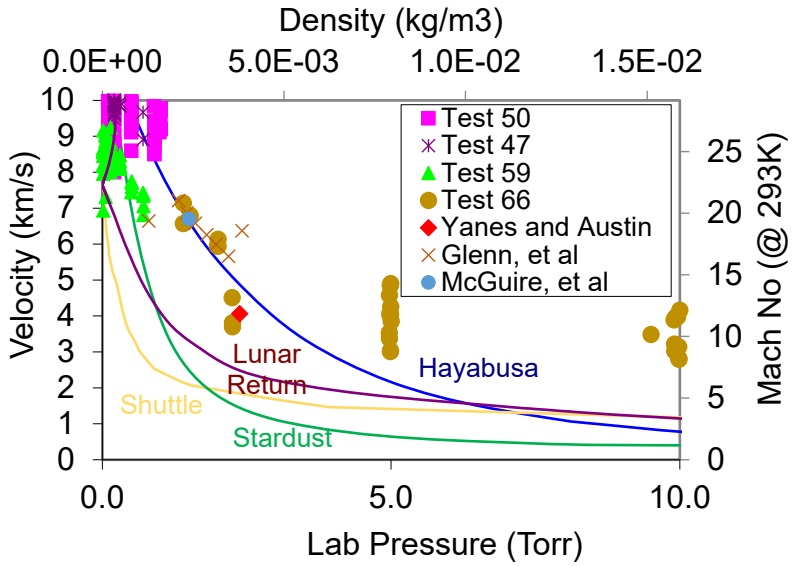

Figure 1. Incident shock test conditions in the current work (Test 66) and previous EAST tests, overlaid with candidate trajectories for various entry vehicles.

II. Experimental

Figure 1 displays the range of incident shock conditions in EAST for the current test series (Test 66) and some previous air test series (Tests 47, 50 and 59). Overlaid on this plot are trajectories from Hayabusa, Stardust and the Space Shuttle, as well as a candidate Lunar Return entry. Equivalent points from experimental facilities previously discussed – HET at CalTech, T6 at Oxford, and Plasma Torch facility at CentraleSupelec are also shown. For the expansion tube, the freestream density and enthalpy have been mapped to their equivalent incident shock velocity and pressure parameters, while the plasma torch temperature and pressure have been converted to the corresponding incident parameters to match post-shock equilibrium. The lower velocity (3-5 km/s) test conditions were chosen to optimize NO formation and included tests at larger nominal pressures of 5 and 10 Torr for this purpose. The condition at 2.25 Torr was chosen to replicate studies related to the HET condition. Among the T6 Test conditions, nominal conditions of 7 km/s, 1.4 Torr and 6 km/s, 2.0 Torr were selected to obtain 1 bar post-shock conditions which could be compared against both T6 and Plasma Torch data. Coincidentally, these points lie very close to the Hayabusa entry trajectory.

The EAST facility has been discussed in previous works [6]. It consists of a 10.16 cm diameter aluminum tube that is filled with test gas at different pressures and separated from an electric arc driver by aluminum or stainless steel diaphragms. In the current work, 0.06-0.09" pre-scored diaphragms are employed which result in less shock deceleration than thin, unscored diaphragms with low burst pressures used in previous test series. The energy for the arc discharge is supplied by a 863 μF capacitor bank at voltages between 6-14 kV. The driver is filled with He at a

nominal pressure of 200 psi and the test gas is hydrocarbon free air. Two turbomolecular pumping stations at either end of the driven tube evacuate the tube to base pressures less than 10^{-5} Torr prior to charging with the test gas. The outgassing rate measured is generally less than 3×10^{-5} Torr/min.

The optical test section is located approximately 6.75 m downstream of the main diaphragm. The major analytical technique employed in the EAST utilizes 4 spectrometers in two vacuum optical boxes coupled to opposite sides of the test section. The spectrometers image the same axial location in the shock tube through a slot window in the test section. The slot windows were either fused silica for measuring UV-NIR wavelengths, or magnesium fluoride for measuring the mid-infrared. Imaging optics translate the axial dimension of the shock tube onto the length of the spectrometer slit. The spectrometer then disperses the signal by wavelength in the horizontal direction, obtaining an image of radiance versus wavelength and axial position. Representative results are shown in Figure 2 and will be discussed below. The signal on the CCD array is converted to units of spectral radiance by calibration against known radiance sources, including integrating sphere (300-1700 nm), D_2 lamp (< 300 nm) and Blackbody (4500-5700 nm) calibration sources [27].

Test conditions and spectrometer settings are summarized in Table 1, which includes the 43 shots performed in the test series and also depicted in Figure 1. Shots that provided no useful data are omitted from the table. The first test condition targeted 3-4 km/s and 10 Torr and will be discussed in Sect. III.B. Measurements in the Vacuum Ultraviolet (<200 nm) were attempted but yielded no useful signal. Ultraviolet and Visible spectrometers were set to cover the range 200-370 nm and 480-890 nm, respectively. The former range measured the UV NO bands while the latter detected weak signal that will be discussed below. Subsequent tests shifted the VUV spectrometer to measure the UV range (approximately 200-400 nm) and the UV/Vis spectrometer to 330-500 nm. The infrared spectrometer was used with the mid-infrared camera from IR Cameras, LLC to monitor the NO infrared band. These same settings were employed for subsequent tests at 5 Torr and 2.25 Torr. For the 1 bar shot conditions, identical settings were employed for the VUV, UV/Vis and Vis/NIR spectrometers, but a Near-infrared (Indigo Phoenix) camera was substituted on the IR spectrometer to measure infrared atomic emission lines as the mid-infrared signal was predicted to be below detection limits. Later in the test series, starting with Shot 36, the Indigo camera was replaced with a WiDy-Sens 640V camera from New Imaging Technologies. This camera could not detect signal below 930 nm, so the spectral range was shifted as shown in Table 1.

III.Results

A. Tests from 3-5 km/s

Representative measurements of this regime are shown in Figure 2. The first three images depict measurements at 4.1 km/s and 5 Torr in the ultraviolet through visible part of the spectrum. The most significant feature is NO radiation in the ultraviolet which is primarily due to the γ ($A\,^2\Sigma^+$-$X\,^2\Pi$) band, but also has some overlap from β ($B\,^2\Pi$-$X^2\,\Pi$) and δ ($C^2\,\Pi$-$X^2\,\Pi$) bands. These features continue out to higher wavelengths at much lower intensities (1 and 2 OOM less on the UV/Vis and Vis/NIR cameras, respectively). Also present within the spectra are the O_2 Schumann-Runge ($B^3\Sigma_u^-$-$X^3\Sigma_g^-$) bands and continuum radiation sources which are not yet identified. The fourth image depicts mid-infrared data at 3.9 km/s and 10 Torr. The mid-infrared camera shows vibrational transitions of NO which, while weak in intensity, are interesting since they probe the molecular ground state.

Table 1. Summary of test conditions

Shot No	Velocity (km/s)	Pressure (Torr)	UV	UV/Vis	Vis/NIR	IR
1	3.48	9.5	150-200 nm	200-370 nm	480-890 nm	5000-5700 nm
2	3.22	9.9				
3	2.82	10.0				
4	2.79	10.0				
5	3.89	9.9				
6	3.97	9.9				
7	3.94	9.9	300-520 nm			
8	3.85	5.0				
9	3.03	5.0	200-400 nm	330-500 nm		
10	3.01	5.0				
11	3.53	5.0				
12	3.37	5.0				
13	4.08	5.0				
14	4.05	5.0				
15	4.04	5.0				
16	4.26	5.0				
17	4.90	5.0				
18	4.85	5.0				
19	4.58	5.0				
20	4.02	5.0				
21	3.98	10.0				
22	4.16	10.0				
23	3.02	9.9				
24	3.14	10.0				
25	3.70	2.3				
26	3.81	2.2				
27	4.51	2.2				
28	5.94	2.0				850-1450 nm
29	5.95	2.0				
30	6.13	2.0				
31	6.57	1.4				
32	6.79	1.5				
33	7.14	1.4				
36	5.89	2.0				930-1450 nm
37	5.99	2.0				930-1570 nm
38	5.97	2.0				
39	6.97	1.4				
40	6.59	1.4				
41	7.03	1.4				
42	6.90	1.4				
43	6.65	1.4				

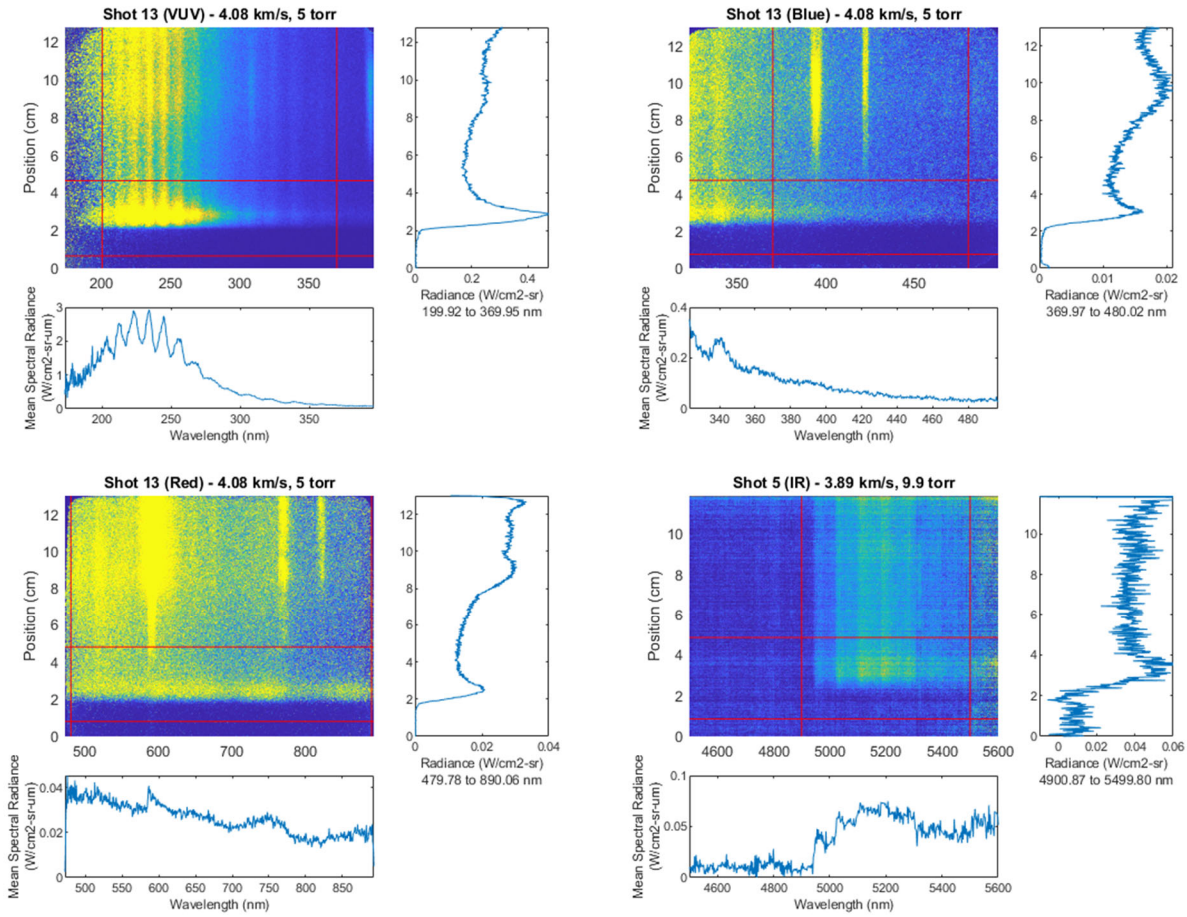

Figure 2. Radiance versus wavelength and position measured in the (a-c) UV to Visible range at 4.1 km/s and 5 Torr and (d) mid-infrared at 3.9 km/s and 10 Torr.

B. 4 km/s, 10 Torr

The nominal freestream condition of 4 km/s and 10 Torr is discussed first, as the post-shock has a reasonable expectation of obtaining equilibrium. The post-shock pressure in these cases is expected to be 2.2 bar. There are 5 shots (5-7, 21-22) which obtained this condition, though only one of them has measured all four wavelength ranges simultaneously. Figure 3 shows the radiance versus position in the ultraviolet (200-370 nm) and infrared (4800-5500 nm) regions. Data is plotted relative to the shock front location determined by time of arrival sensors, except for shot 5 where no time of arrival data was obtained, shot 7 UV which required a 1.6 mm manual adjustment, and shot 6 IR which had no camera trigger data. All 5 shots obtained data in the UV (albeit with different cameras as seen in Table 1), but only 3 shots had IR data. The UV data is truncated at 4 cm where contamination radiation becomes significant but shows a relatively flat plateau from 1-4 cm on all cameras. The infrared data displayed a plateau from about 2-6 cm. The shock moves approximately 0.8 cm during the camera exposure time, which explains most of the observed rise and fall time – the non-equilibrium feature is likely much narrower than the data appears to indicate. The ultraviolet intensity is increasing monotonically with velocity. However, the rate of increase is larger than would be expected based on equilibrium considerations as will be discussed. The infrared data is relatively consistent across the three shocks measured, but slightly higher on shot 6.

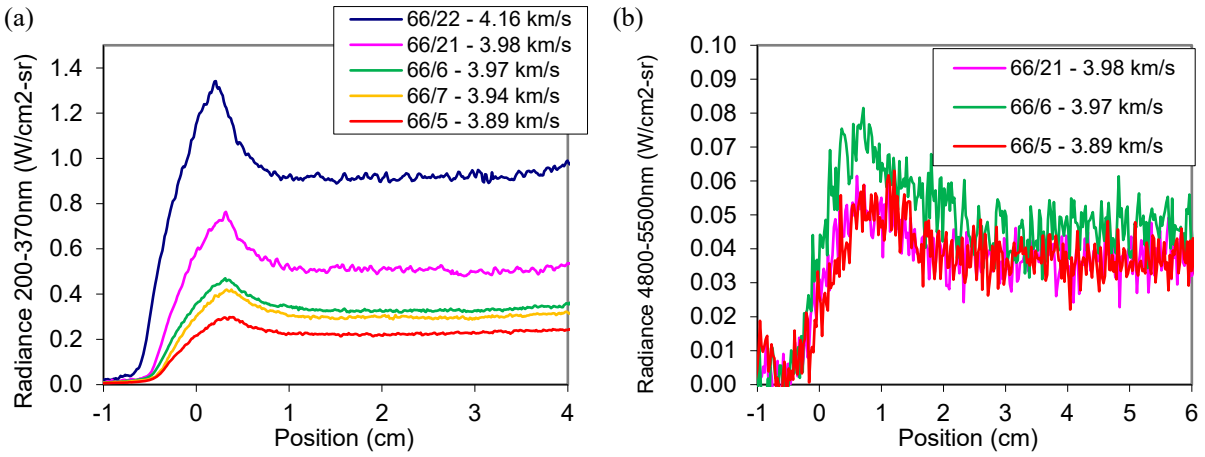

Figure 3. Radiance versus position at 4 km/s (nominal) and 10 Torr.

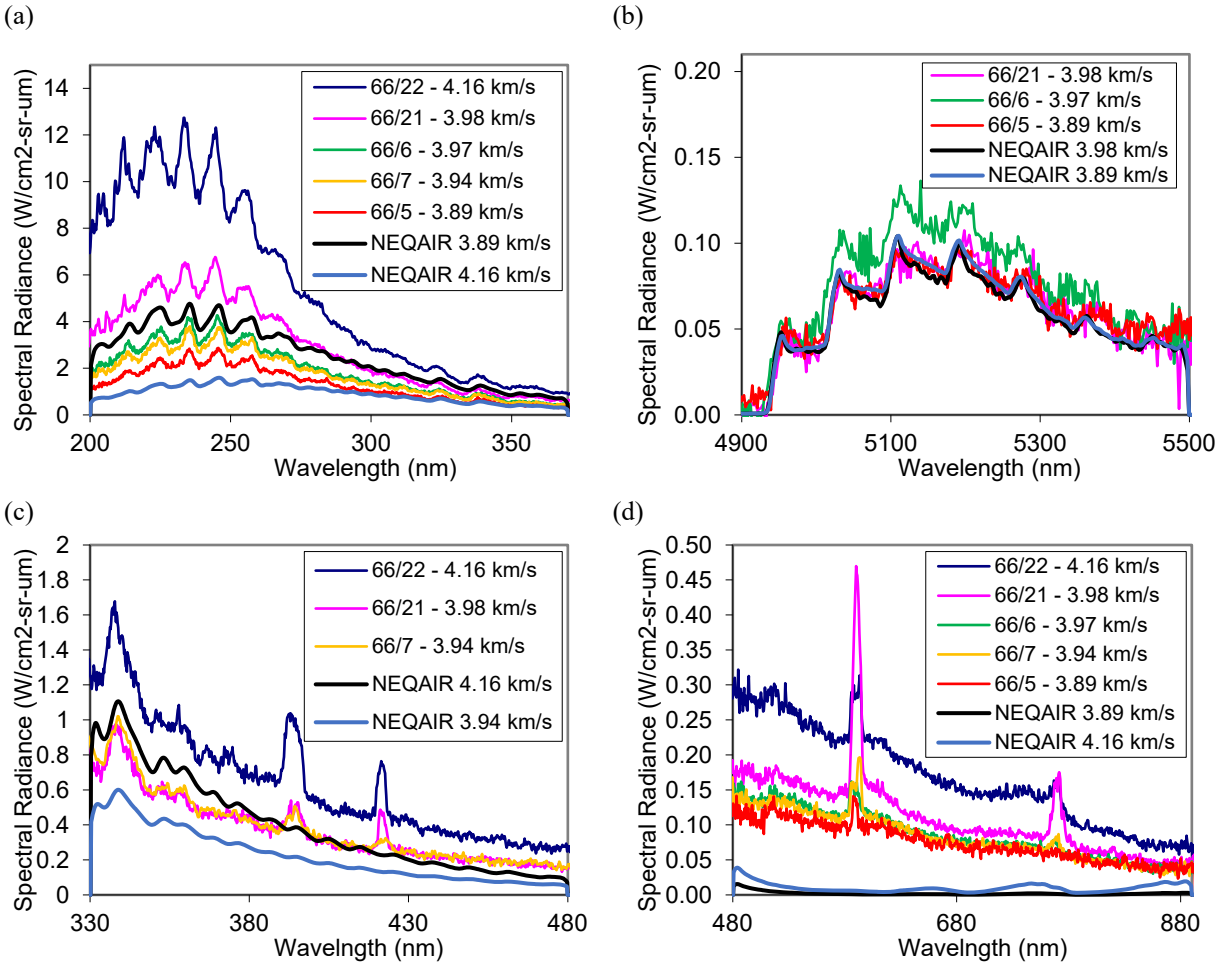

Figure 4. Equilibrium spectral radiance at 4 km/s and 10 Torr. (a) Ultraviolet, (b) Infrared, (c) near-UV, (d) Vis-Near IR

Figure 4 shows radiation in the equilibrium region for the UV and IR cameras, along with corresponding NEQAIR predictions. The NEQAIR predictions shown are based on NEQAIR 15.3 [28], using inputs generated by

the Chemical Equilibrium and Applications (CEA) [29] code for incident shock equilibrium. Rotational, vibrational and electronic states are assumed to be Boltzmann distributed at the equilibrium temperature. In the infrared, NEQAIR simulations at 3.89 and 3.98 km/s yield very similar results and are in good agreement with shot 5 and 21 data. Shot 6, which is similar in velocity to shot 21, is about 30% higher than both the NEQAIR result and the other data. The agreement suggests that a post-shock equilibrium state may be obtained.

However, the ultraviolet spectra, shown in Figure 4(a), do not in general show agreement with equilibrium radiation predictions. The UV radiance increases monotonically with velocity. Two NEQAIR simulations are overlaid at both the lowest and the highest velocity. In both cases, the spectrum is underpredicted. The measurement is between 30 and 300% larger than the NEQAIR prediction, with the agreement being worse at lower wavelength and higher velocity. The higher velocity cases with larger discrepancy were obtained later in the test series. A large jump in intensity is seen between shots 6 and 21 even though the velocity change is only 0.01 km/s. While a different spectrometer/camera pair was utilized on shots 5-7 and 21-22, this change could be due physical phenomena. Possible reasons for these discrepancies will be discussed below.

Measurements in the UV/Vis (or near-UV) and Vis/NIR ranges of the EAST spectrometers are shown in Figure 4(c) and (d). The UV/Vis spectrum is an order of magnitude weaker than the UV spectrum and the visible spectrum is yet another order weaker than that. The near-UV spectrum shows similar results in shot 7 and 21, with shot 22 being somewhat higher. A significant amount of this difference can be attributed to the higher velocity, as demonstrated by the two NEQAIR results. NEQAIR does, however, underpredict the level of radiance in this region. This difference is nearly constant over the UV range at ~0.1 W/cm^2 at the lower velocities and ~0.2 W/cm^2 at the highest velocity. The visible to near-IR region has similar radiation magnitudes between shots 5-7, with a somewhat higher radiation in shots 21 and 22. NEQAIR underpredicts the level of radiance in this region and displays less velocity dependence than in the ultraviolet. The NEQAIR prediction is mostly between 1-2 orders of magnitude lower than the measurement.

Table 2. Contamination levels deduced from spectra in parts per billion (ppb). *indicates a maximum value since Al and Ca+ cannot be distinguished at the instrument resolution. NM=not measured.

Shot No	Na	K	Ca	Al*	Ca+*
5	0.8	<0.1	NM	NM	NM
6	1.0	0.2	NM	NM	NM
7	1.4	0.3	0.9	50.7	7.0
21	2.2	0.4	3.2	61.5	8.9
22	1.2	0.3	2.6	105.6	17.7

The spectra in the UV/Vis and Vis/NIR regions display noticeable signal from contaminant species. Features from 394-396 nm are blended Ca^+ and/or Al lines that are not distinguished at the spectral resolution employed. Peaks at 592 and 771 nm are attributed to Na and K, respectively. The line at 421 nm is from the Ca neutral. Potassium, calcium and sodium are well known contamination features in ground facilities. Aluminum features can come from the primary diaphragm or the tube wall. While the Na (and sometimes K) features are present in the shock from the very beginning, the Al/Ca features are not observed until sometime following the shock front, but still within the plateau region. This suggests the Na/K is persistent throughout the tube while the Al/Ca is a temporal feature traveling with the shock. At the completion of the tests, it was found that an upstream instrumentation port had been installed incorrectly, introducing aluminum erosion into the tube and is a possible source of early contamination. However, concurrent laser absorption spectroscopy measurements [15] were not noticeably altered at the time the Al was observed. Clear transitions in laser signal corresponding to the contact surface are seen between 30-40 μs (12-16 cm) after the shock front. From the intensity of the contamination lines, it is possible to estimate a species number density assuming the atoms follow a Boltzmann distribution at the post-shock equilibrium temperature. Concentrations estimated in this way are shown in Table 2. The contaminations are not large, with Na, K and Ca being at the ppb level. Al and Ca^+ cannot be clearly distinguished so the levels reported are those obtained assuming only one or the other is present – thus representing an upper bound of the contamination. These species are less than 100 ppb. The Na, K and Ca levels are somewhat elevated in Shot 21 compared to the others, while Al/Ca^+ is higher in the higher velocity (and more luminous) shots. Based on the equilibrium temperature and electron density in these shots, Saha equilibrium would predict impurity ionization levels that are higher than the corresponding neutral densities (up to 20× for Na and 200× for K). This could raise the ionization level by as much as 5% in the shock. Bound-free cross-sections for these species [30] were implemented in NEQAIR and run assuming Saha equilibrium, but the impact is orders of magnitude lower than the measured radiation. While these

species then cannot directly explain the excess radiance, it is possible that some interactions of the electronic states with these contaminants may play a role.

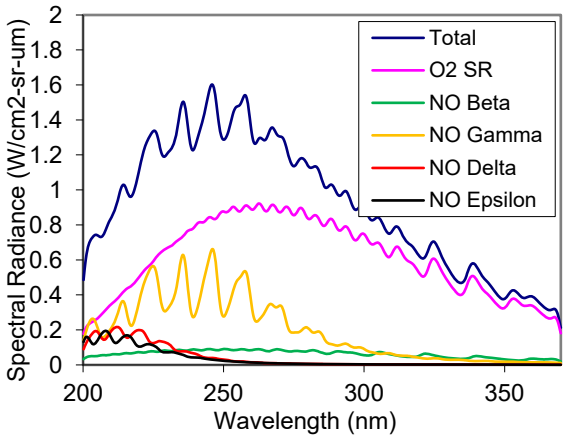

Figure 5. Band contributions at 3.89 km/s, 10 Torr (Shot 5).

NEQAIR prediction of radiation in the ultraviolet is attributable to the O_2 Schumann-Runge ($B^3\Sigma_u^-$-$X^3\Sigma_g^-$) system and various bands of NO as shown in Figure 5. The NO radiation includes contributions from the so-called γ ($A^2\Sigma^+$-$X^2\Pi$), β ($B^2\Pi$-$X^2\Pi$), δ ($C^2\Pi$-$X^2\Pi$), ε ($D^2\Sigma^+$-$X^2\Pi$), β′ ($B'^2\Delta$-$X^2\Pi$), and γ′ ($E^2\Sigma^+$-$X^2\Pi$) bands, although the last two are negligible for this condition. While the discrepancy in intensity could indicate an overpopulation of some of these excited states, additional sources of radiation intensity not currently modeled in NEQAIR should also be considered. The predicted Schumann-Runge bands only includes transitions between bound levels. In absorption, photodissociation of O_2 produces the Schumann-Runge continuum, which drops sharply above 170 nm at room temperature. However, at elevated temperature as higher rotational and vibrational levels of O_2 become populated, absorption may be observed into the ultraviolet and higher wavelengths.[31, 32] At sufficiently high temperature and O atom density, the reverse process, i.e. photorecombination, should be observed in emission:

$$O + O \rightarrow O_2 + h\nu \tag{1}$$

To incorporate this into NEQAIR, cross-sections for O_2 photodissociation were computed using the PyDiatomic code from ANU [33]. Provided with the code are potential energy curves and dipole moments for O_2 $X^3\Sigma_g^-$ and $B^3\Sigma_u^-$, as well as several antibonding Σ and Π states with their couplings. Additional details may be found in [34, 35]. Cross-sections from individual j, v levels of $O_2(X)$ are computed and summed over a Boltzmann weighting to obtain the total absorption cross-section:

$$\sigma_{ab}(\lambda,T) = \frac{\sum_{j,v}\sigma_{jv}(\lambda)(2J+1)e^{-E_{jv}/kT}}{\sum_{j,v}(2J+1)e^{-E_{jv}/kT}} \tag{2}$$

where nuclear degeneracy alternation has been neglected. The denominator is recognized as the rovibrational partition function of the $X^3\Sigma_g^-$ state.

The photorecombination cross-section may be related to the photodissociation cross-section through detailed balance. Per Kirchoff's law of radiation, the radiation produced by photorecombination and photodissociation at equilibrium must yield the Planck function in the optically thick limit. Applying this relationship yields equations for spontaneous and stimulated emission from the absorbance cross-section. We can therefore write the absorption and emission coefficients as:

$$a = \sigma_{ab}(\lambda,T)\left(n_{O2(X)} - \frac{n_O{}^2}{K_{eq}^*}e^{-hc/\lambda kT}\right) \tag{3}$$

$$e = \sigma_{ab}(\lambda, T)\frac{2hc^2}{\lambda^5}\frac{{n_O}^2}{K_{eq}^*}e^{-hc/\lambda kT}$$

Since the absorption cross-section here describes dissociation from the molecular ground state, the rate must be proportional to the O_2 ground state density, which differs by about 5% from the O_2 molecular density. Correspondingly, the equilibrium coefficient, K_{eq}^* must be written relative to the ground state of O_2, i.e.

$$K_{eq}^* = \frac{{Q_O}^2}{Q_{O2(X)}}e^{-E_0/kT} \tag{4}$$

where the total partition functions include translation, nuclear and electronic degeneracy for atoms and molecules, and rovibration for $O_2(X)$. Technically, the O atom densities in the calculation should correspond to the densities of the dissociation product state(s). The equilibrium constant would then be expressed relative to those states (i.e. using electronic degeneracies instead of electronic partition functions). If the atoms are Boltzmann distributed, these modifications offset each other, yielding an identical relation to eq. (3). For a non-Boltzmann distribution, eq. (3) is still expected to be a good approximation since the process is dominated by lower energy states whose population may be described by the effective temperature. The absorption cross-sections have been calculated over a range of temperatures as described by eq. (2) and provided as a database file to NEQAIR. NEQAIR performs interpolation of the cross-section to the temperature of interest and uses eq. (3) and (4) to derive the emission and absorption coefficients. At present, only a single temperature model of photo-recombination/dissociation is employed. Eq. (2) can be modified to account for separate rotational and vibrational temperatures for the absorption rate. Detailed balance predicts that the emission rates (both spontaneous and stimulated) would be only a function of T and T_{el}.

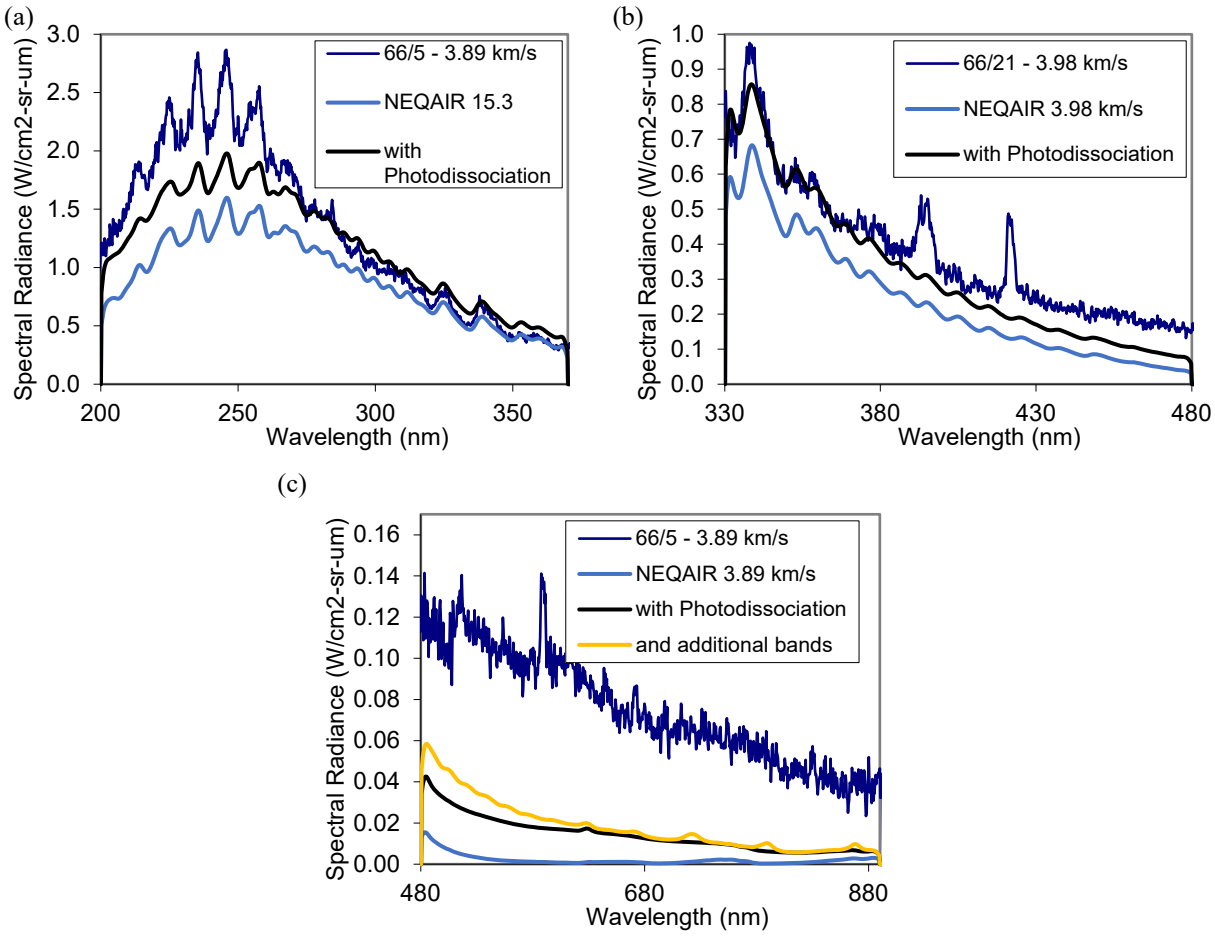

Figure 6. Comparison of EAST to NEQAIR with and without O2 photorecombination at 4 km/s and 10 Torr

The impact of photorecombination on the equilibrium comparisons is shown in Figure 6. The photorecombination has improved the agreement overall. The UV region below 280 nm is still underpredicted but by a lesser amount. From 280-370 nm, shot 5 is somewhat overpredicted while Shot 21 shows good agreement from 330-370 nm. At higher wavelength up to 890 nm (the limits of the EAST measurement), the photorecombination has a noticeable impact on the spectrum. The experimental radiation remains underpredicted however the prediction is now within an order of magnitude of the measured signal. In the ultraviolet, the photodissociation cross-sections obtained in this work differ in both magnitude and shape to those computed by Bykova and Kustova [32], but are mostly within a factor of two. We are not aware of any comparable photorecombination data out to 900 nm. Therefore, there is likely room for improvement in the photorecombination calculation, but whether it could resolve the remaining discrepancies is unclear. To test for other sources of radiation, the NO Ogawa ($b^4\Sigma^-$-$a^4\Pi$) and Heath ($C^2\Pi$-$A^2\Sigma^+$) bands were implemented in NEQAIR, the bound O_2 Schumann Runge bands were extended from a maximum v″ of 21 to 30 and the NO β bands extended from v′=15, v″=21 to v′=21, v″=32. These changes only had a noticeable impact in the visible, shown in Figure 6(c), where the Schumann-Runge intensity has increased from 500-600 nm and small features attributable to the Ogawa bands are visible from 700-900 nm.

Because much of the ultraviolet spectrum is optically thick, the intensity measured at low resolution may show sensitivity to what may often be considered second order effects in the molecular spectra. Line broadening and line splitting may distribute the radiation more uniformly over wavelength such that self-absorption is reduced and the mean spectral intensity is increased, while the shape of band is not significantly altered. The impact of updating these parameters in NEQAIR is shown in Figure 7. Line splitting is not enabled by default in NEQAIR but can be activated through environment variable. Enabling this feature increases the peak UV radiance by approximately 8%. Splitting constants for O_2 are not included in the NEQAIR 15.3 database so needed to be updated. The NEQAIR Hamiltonian differs from that employed in the literature for O_2, requiring a transformation of the constants. The spin-rotation (γ_{NEQ}) and spin-spin (ε_{NEQ}) constants employed are related to the O_2 constants approximately as:

$$\gamma_{NEQ} = -2\gamma_{O2} \tag{5}$$

$$\varepsilon_{NEQ} = \frac{2\lambda_{O2}}{3} - B$$

Furthermore, the NEQAIR constants are only evaluated to first order, so do not include variations with respect to vibrational level or a higher order polynomial term in J(J+1). The higher order terms are thus neglected and a representative value across the bands for γ_{O2} and λ_{O2} are chosen from the literature [36, 37]. The resultant values employed are γ_{NEQ}=1.7 x 10^{-4} cm^{-1} and ε_{NEQ}=1.34 cm^{-1} for the ground state and γ_{NEQ}=5 x 10^{-2} cm^{-1} and ε_{NEQ}=0.4 cm^{-1} for the B state. The impact of these constants is an additional 8% increase in peak radiation. The impact of line broadening parameters are also examined. By default, NEQAIR uses Griem's formula [38] for van der Waals broadening of atoms and a single value proportional to λ^2 (i.e. constant in wavenumber) for all molecular lines. Enabling Griem's formula for molecules increased the radiation by an additional 6%. Predissociation linewidths [39] are not currently included in NEQAIR, so the linewidth was implemented based on its relationship to the predissociation lifetime, τ:

$$\Delta\lambda_{prediss} = \frac{\lambda^2}{2\pi c\tau} \tag{6}$$

Technically τ is dependent upon both J and v. Average values of τ are included in NEQAIR's non-Boltzmann database. For expediency this single value of τ is employed for the entire band. Primarily this impacts the O_2 SR and NO δ bands, whose upper states have significant predissociation rates. This increases the radiance by an additional 2%. It is noted that adding additional sources of broadening and splitting comes with diminishing returns as the effects are less than additive. Any one of these mechanisms taken in isolation may have an impact of 10% more, but the cumulative effect of all of them have been to increase the peak radiance by 26%. The spectrum is now in reasonable agreement, being somewhat underpredicted at the peak and overpredicted at longer wavelengths. These changes had minimal effect on radiation at higher wavelengths.

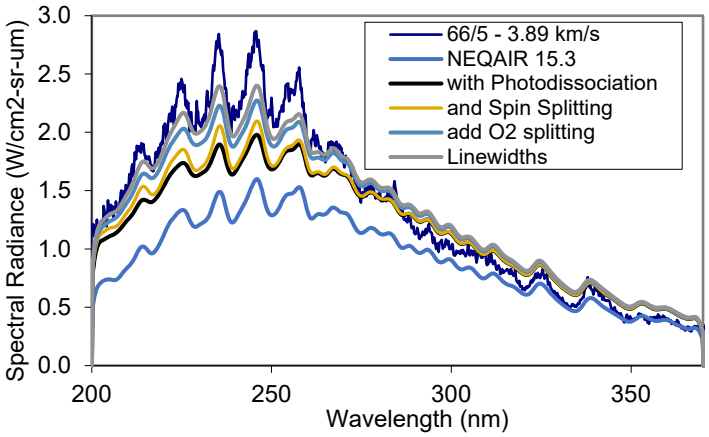

Figure 7. Impact of fine structure modification on ultraviolet radiation. 4 km/s, 10 Torr.

The remaining discrepancy in the spectrum may be accounted for by adjusting state densities, however there is not a unique combination that matches the data. For instance, increasing the density of NO(A) by a factor of 2, while decreasing O_2(B) and NO(C) by 22 and 14%, provides a good agreement. The reduction in O_2(B) and NO(C) could be caused by pre-dissociation and is approximately in the right ratio to be explained by a lowered O atom concentration. However, reducing the O atom concentration also lowers the photorecombination contribution and requires other parameters to be increased to offset this effect. A fit was performed using NEQAIR's non-Boltzmann model, which computes a balance between excitation, dissociation and radiation. Allowing heavy particle reactions to equilibrate at an independent T_e, an electronic temperature of 4450 K (about 300K above equilibrium), a 20% reduction in O atom concentration and 80% increase in O_2 concentration would reproduce the experimental result. Since this result does not conserve O atoms in the flow, it is not considered to be a physical solution, but gives an indication in the level of deviation from equilibrium represented by the data. A more accurate fit would likely require a more accurate photorecombination cross-section than is currently employed.

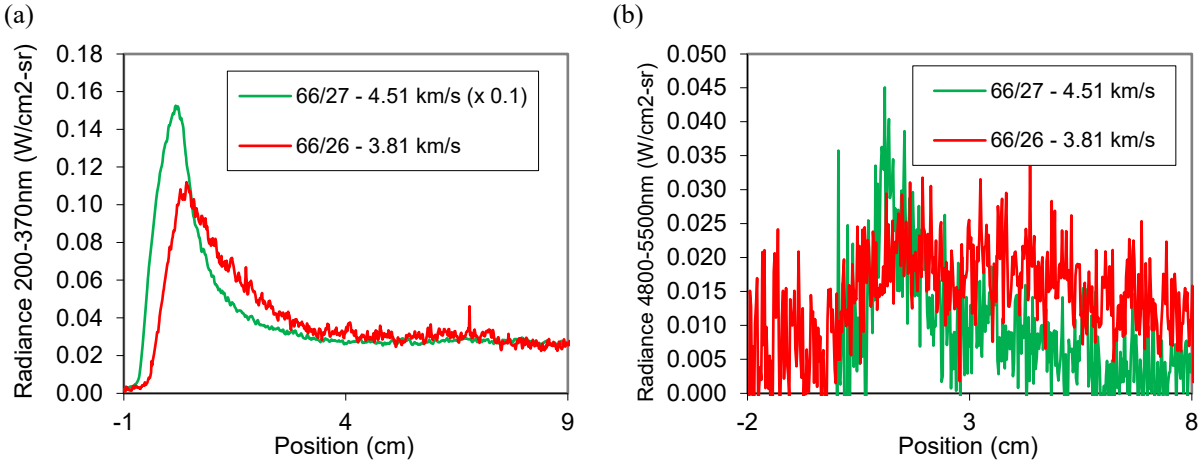

Figure 8. Radiance versus position at the 2.25 Torr condition and two velocities. (a) ultraviolet, (b) mid-infrared

C. 4 km/s, 2.25 Torr

The nominal condition of 4 km/s and 2.25 Torr was chosen to have similarity to the conditions reported by Yanes and Austin [16] and modeled by Karpuzcu, et al.[19] TDLAS measurements of these shots have been reported by Chang, et al. [15] and corresponding DSMC predictions reported by Thirani, et al.[22] Three shots were obtained in this test series, spanning from 3.7-4.5 km/s. Shot 25 did not obtain the full range of UV or any IR data. Figure 8 shows the temporal trends of UV and IR radiation from Shots 26 and 27. The infrared data is compromised by signal to noise ratio. An increase above the baseline level is seen at the shock front, followed by some relaxation which is obscured by the noise. The peak levels are higher at 4.5 km/s than 3.8 km/s, but the relative signal at up to 8 cm

behind the shock has reversed. The ultraviolet spectrum on the other hand is about 10x stronger at 4.5 km/s than at 3.8 km/s. Both cases plateau to nearly constant values at about 3 cm, then remain steady out to 9 cm. While the UV spectra displays no evidence of contamination, the near-UV to Visible ranges (not shown) display contamination approximately 4 cm after the shock front. While the emission spectra appear to obtain a nearly constant value, both TDLAS data and predictions at 3.8 km/s [15, 22] indicate that chemical equilibrium is not achieved, and the flow is relaxing slowly throughout the test time (about 30 μs or 11.4 cm).

In Figure 8 we show comparison to equilibrium predictions at 3.81 km/s for data taken between 3-5 cm behind the shock on all four cameras. Equilibrium predictions are lower than the measurement at all wavelengths. The impact of photorecombination and database updates on equilibrium radiation is shown from 330-890 nm, but omitted from the ultraviolet plot. Photodissociation has increased the prediction by about 20% from 240-370 nm and by a greater amount outside of this wavelength range. Spin splitting increases radiance by up to 10% between 200-280 nm. Modifying the linewidths does not have more than a few percent impact, however. The infrared spectrum displayed an offset in radiance of approximately 11 mW/cm^2-sr-μm that was manually removed. While equilibrium (at 3820K and 3.2 × 10^{16} cm^{-3} of NO) underpredicts the infrared signal, a two-temperature fit of the infrared spectrum yields an NO number density of 6 × 10^{16} cm^{-3}, T_r of 3350 K and T_v of 4040 K. These stand in contrast to TDLAS measurements which yielded 4 × 10^{16} cm^{-3}, 5200 K and 4600 K respectively. Using these measurements as input to NEQAIR yields the curve labeled "TDLAS input." The TDLAS generated spectrum shows reasonable agreement below 5050 nm which corresponds to v′=1. The band turning points for v′=2-4 are also in good agreement. The TDLAS data has probed up to v″=3 and J″=58.5 while the turning point occurs near J=80. A significant overpopulation at large J could resolve the discrepancy, but it is not clear how plausible this would be.

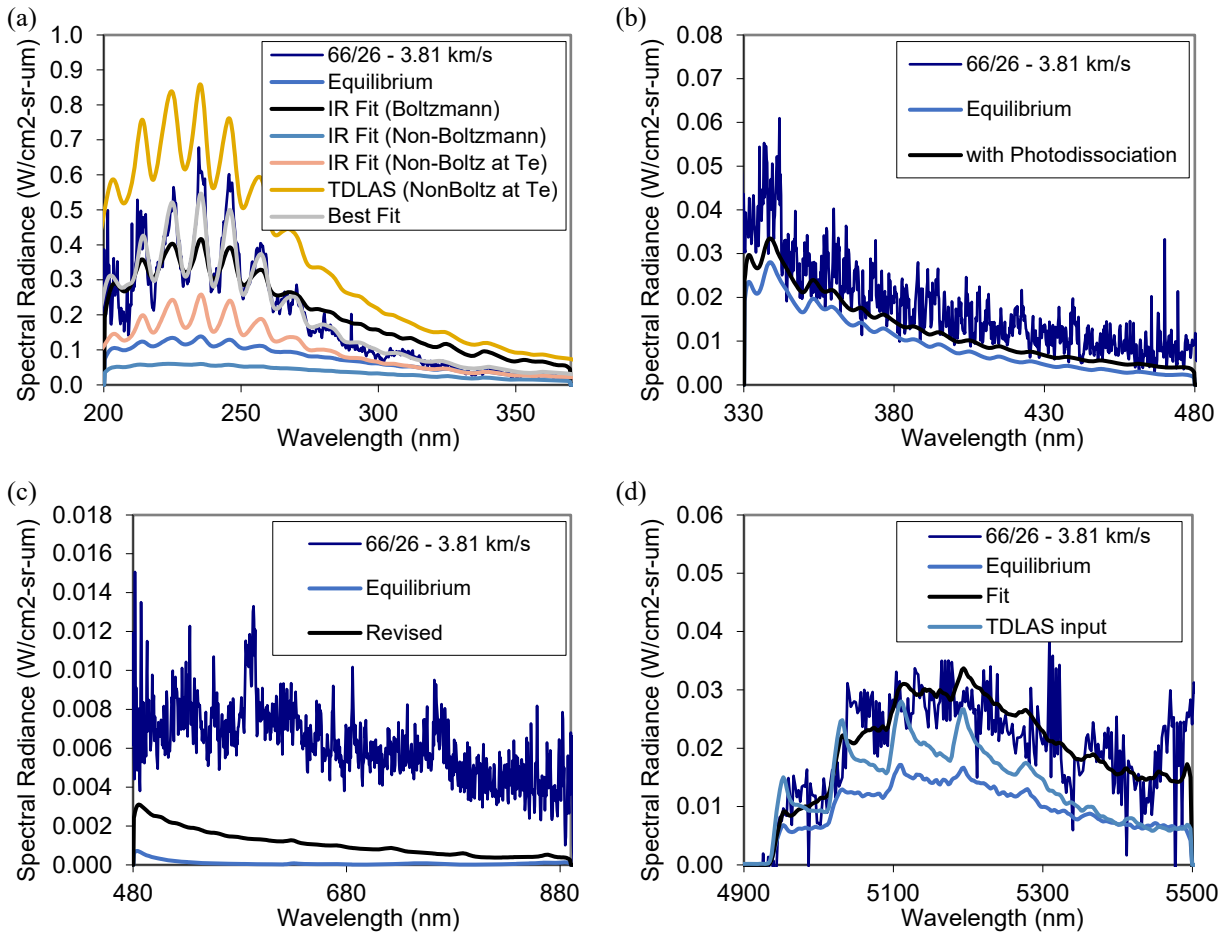

Figure 9. Spectral measurement from 3-5 cm behind the shock front and comparison to various NEQAIR predictions. Conditions are 2.25 Torr and 3.81 km/s.

The spectrum predicted by NEQAIR using the NO IR fit parameters as input is overlaid on the UV plot for both Boltzmann and non-Boltzmann models. While the average level of radiance is close for the Boltzmann model, the peak UV contribution is underpredicted and higher wavelength range overpredicted. The non-Boltzmann model predicts much weaker NO radiation because the heavy particle collisions equilibrate at T_t, which is lower than equilibrium in the IR fit. If instead the heavy particles are set to equilibrate at T_e (assumed equal to T_v) the result lies between the previous two cases. The high wavelength range is no longer overpredicted, though the NO peaks remain underpredicted. Also shown is the non-Boltzmann result, with heavy particles at T_v, using the TDLAS data as input. This result is overpredicted. Using TDLAS input with Boltzmann or heavy particle collisions at T_t gives larger overpredictions and are not shown. Also shown is a fit of the data allowing T_e, O, NO(C) and O_2(B) concentrations to vary while NO density, T_r and T_v are fixed at the IR fit parameters and other densities are set at equilibrium values. This obtains a fit T_e of 4270K. The other parameters are obtained without confidence but are lower than their equilibrium values. The densities of O_2 (B) and NO (C) states may be expected to be lowered due to predissociation. The increased electronic temperature serves to increase the density of NO(A) and other states.

The spectra behind the shock for infrared and UV curves have been fit with results shown in Figure 10. To obtain the fits, spectra are averaged over 50 pixel rows, giving average spectra at 1.2 cm intervals in the infrared and 0.6 cm in the UV. The spectral fits in the infrared give T_r, T_v and NO number density. Near the shock front, T_v peaks at around 7000K, while T_r rises from an initially low value toward equilibrium. This trend is the opposite of typical post shock behavior, where T_v trails the translational temperature. This result is expected for NO because the Zeldovich exchange reactions are known to form vibrationally hot NO molecules.[40] This peak relaxes over approximately 2 cm before it plateaus near 4500K. The rotational temperature remains offset from the vibrational temperature by about 500K. The vibrational temperature drops to the equilibrium value after about 5 cm. The NO number density rises during the vibrational relaxation, overshoots slightly then falls to about 6 x 10^{16} cm^{-3}. This is in excess of equilibrium by nearly a factor of two, suggesting that the reaction kinetics have not yet gone to completion in spite of the relatively steady profile. The post shock profile in the UV is fit using the IR parameters as input for T_r, T_v and n_{NO}. While Figure 9 could be fit with a single T_e if NO(C) and O_2(B) concentrations were reduced, the thermal non-equilibrium region also requires a reduction in NO(B) and NO(D) state densities to match the spectrum. Therefore all state populations are fit independently. The electronic temperature reported in Fig 10 is representative of the relative concentrations of the NO(A) and NO(X) states. This electronic temperature reaches a maximum of 4800K, then tracks the vibrational temperature. Because the system consists of several broad and overlapping bands, the uncertainty in other state populations is typically larger than their fit populations, so these values are not reported. Figure 10(b) shows the NO(A) state density (scaled by 10^6) alongside the NO(X) concentration from the infrared. At around 5 cm, where the vibrational temperature abruptly shifts, a feature attributed to the OH Meinel (A-X) system is observed at 310 nm. Densities responsible for this feature would correspond to less than 100 ppm of the gas mixture.

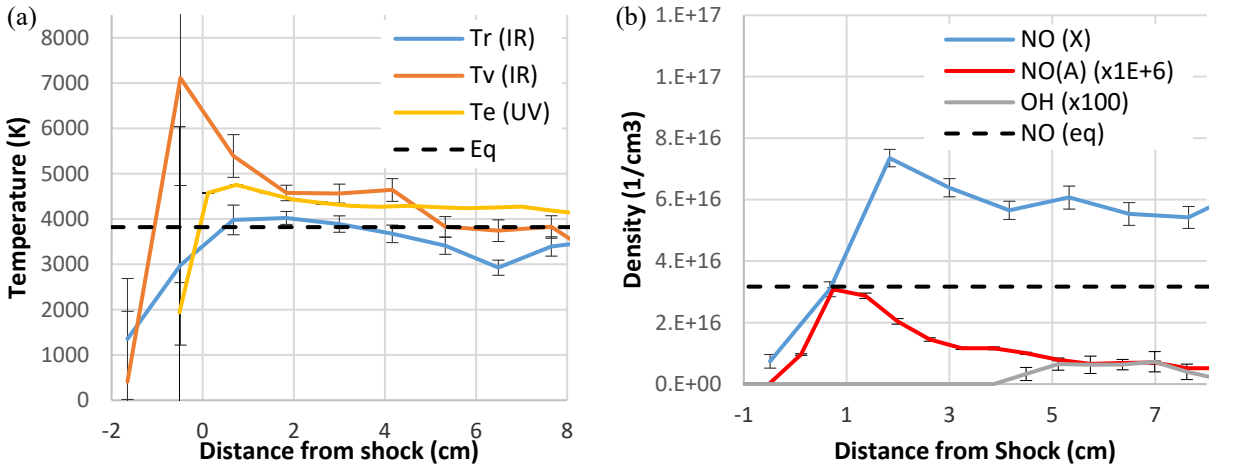

Figure 10. Estimated profiles behind the shock at 3.81 km/s and 2.25 Torr. (a) Temperature, (b) Number densities

The number densities obtained from analysis of this shot are in rough agreement with DSMC predictions of this test. [22] They however are in excess of and slightly outside the error bounds of the concurrent TDLAS measurements. They are also somewhat in excess of CFD predictions of the same [15]. The rotational temperatures do not follow those reported in either of these studies, which start between 5500-6500K then relax to be in the range of 4500-5000K

at the completion of the test. The vibrational temperature is in reasonable agreement with both the DSMC and TDLAS measurements after 2 cm, although TDLAS does not detect a peak in T_v at the shock front.

D. 6.0 km/s, 2.0 Torr

The 6 km/s, 2.0 Torr condition in the EAST facility obtains a post-shock pressure of approximately 1 bar. It is similar to the shot 201 condition obtained in Oxford T6 at 5.97 km/s and 1.96 Torr [26]. Radiance as a function of distance behind the shock front is shown in Figure 11 over two spectral ranges which were also measured in the T6 test. The T6 data has been scaled by 0.45 to account for differences in tube diameter (22.5 cm vs. 10.2 cm). Six shots were obtained in the EAST facility at this nominal condition (shots 28-30 and 36-38). Shots 28,37-38 used a smaller slit setting of 100-120 μm while shots 29-30,36 used a coarser 250 μm slit. Shot 38 used a short exposure time of 0.5 μs to obtain a higher spatial resolution, while the remaining shots used a 1 μs exposure. Shot 38 also performed a 2x2 hardware binning which reduced the effective camera size to 512 x 512 pixels. The T6 results employed a 100 μm slit, 0.5 μs exposure in the visible and 1.0 μs in the ultraviolet. Signal levels in the EAST tests show significant variation in the ultraviolet. Shot 29 is consistently higher and Shot 28 lower than the other tests across all the cameras, so are discarded as outliers in further discussion. In the ultraviolet, shot 30 is also low while shots 36 and 38 give similar magnitudes. Shots 37 and 38 show a rising signal after ~4 cm which is due to contamination, while shot 36 is relatively clean with less post-shock spatial variation. The T6 data lies between shot 37 and shot 28/36 data immediately behind the shock. In the visible range, the amount of scatter in the data is less. Excluding the two outliers, the remaining four EAST shocks are relatively consistent with each other and the T6 data. All of these measurements lie between 0.25-0.30 W/cm^2-sr.

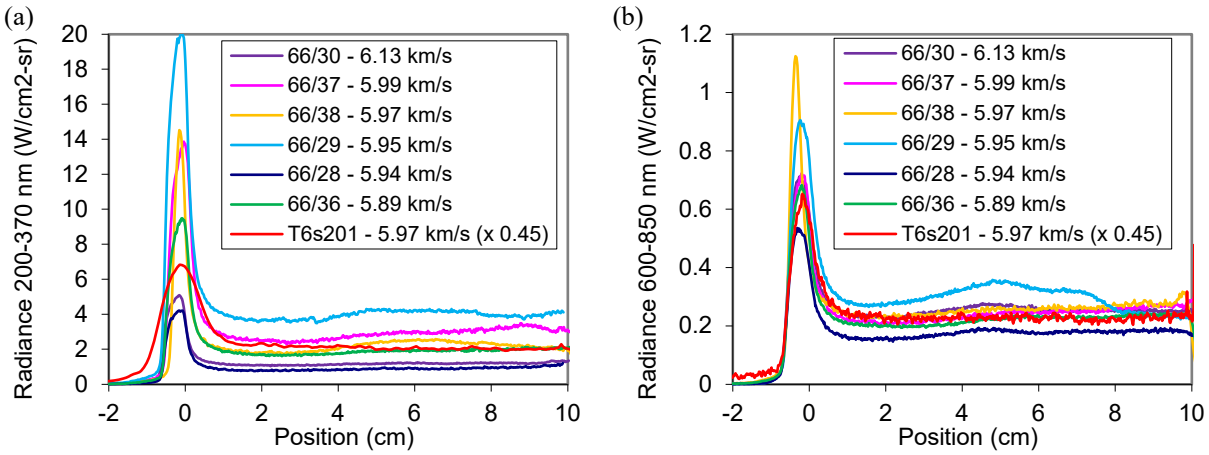

Figure 11. Radiance versus position behind shock front at 6 km/s and 2 Torr.

Discarding the highest and lowest signals measured, the remaining four shocks are compared spectrally from approximately 1-3 cm behind the shock front in Figure 12. In the ultraviolet, the T6 result shows similar magnitude to Shot 37 at the high and low wavelength ends of the spectrum and is nearer to shots 36 and 38 in the intermediate ranges. The equilibrium condition predicted by NEQAIR is lower than all the EAST and T6 measurements. Photorecombination increases the UV radiance by 10-20%, making it lie on top of the spectrum obtained for shot 30. This is still substantially lower than the median radiation level from the EAST testing. In the near-UV to visible range (330-480 nm), the EAST spectra are more self-consistent but still significantly above equilibrium. In the visible range (480-890 nm) the EAST spectra and the T6 spectrum are in very good agreement for most of the range measured. The T6 data begins to deviate from the EAST tests above 850 nm. The equilibrium spectrum in this range is again underpredicted, but by a lesser amount at higher wavelengths. In this regime, the photorecomibination no longer has an impact on the spectrum so is not shown. In the infrared, EAST data appears consistent from all shots obtained, and is in agreement with equilibrium predictions near 870 (N_2 1st Positive, $B^3\Pi_g$-$X^1\Sigma_g^+$) and 1220 nm (NO Heath, $C^2\Pi$-$A^2\Sigma^+$). Features observed from 950 to 1150 nm are not predicted by NEQAIR, and may be attributed to transitions between excited electronic states of NO [41].

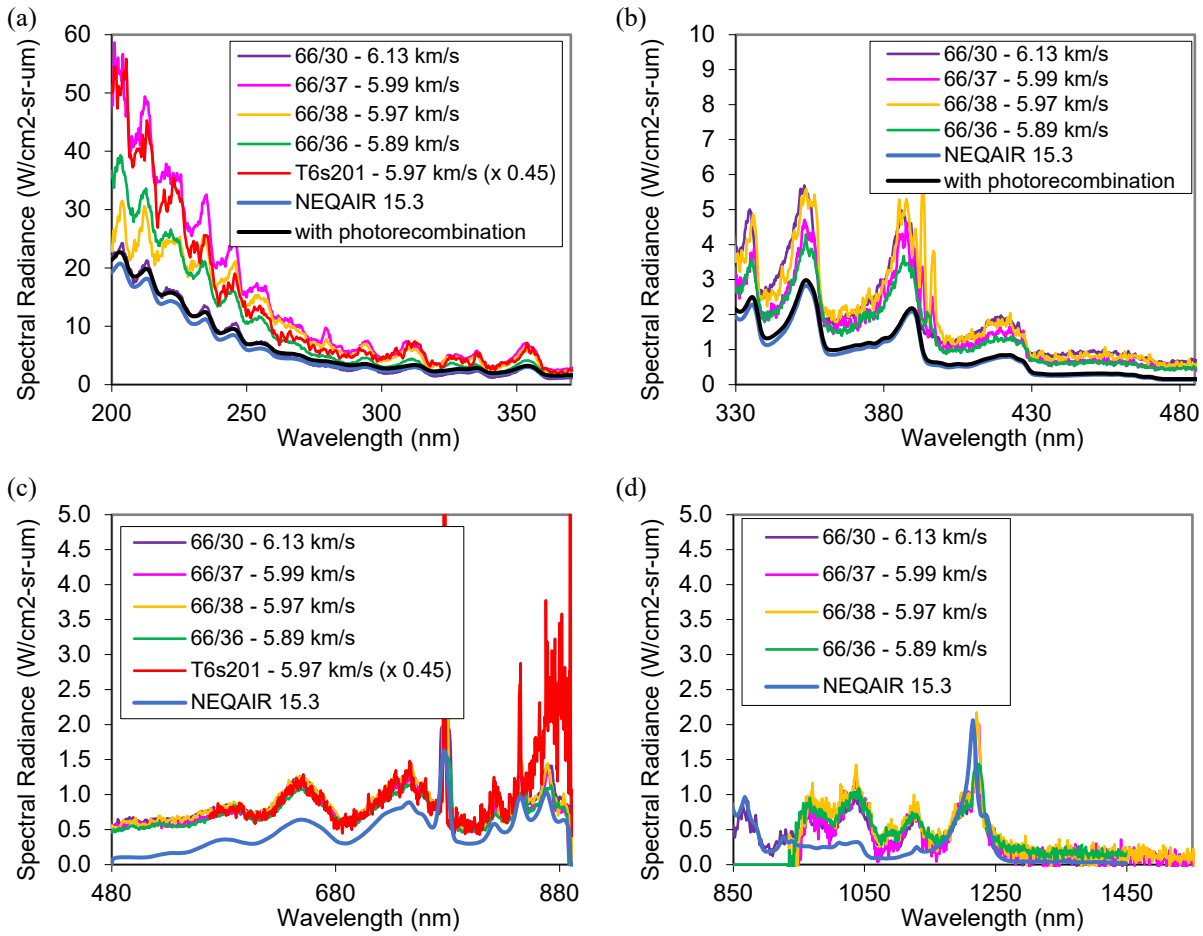

Figure 12. Comparison of spectra at 6 km/s and 2.0 Torr obtained in EAST and Oxford T6 facilities. Also shown are corresponding equilibrium predictions.

E. 7.1 km/s, 1.4 Torr

The 7.1 km/s and 1.4 Torr condition is the second condition chosen to reproduce a spectrum at 1 bar post-shock that can be compared against comparable data collected in the Oxford T6 facility. In the EAST tests, four shots (33, 39, 41 and 42) were obtained at this nominal condition, spanning 6.90-7.14 km/s. Figure 14(a) and (b) compare the radiance magnitude behind the shock in two spectral regions – ultraviolet from 200-370 nm and visible from 600-850 nm. These spectral regions are within the ranges of the T6 data, which is co-plotted. The T6 condition is close in velocity to shot 33 at 7.12 km/s, but at a lower pressure of 1.32 Torr. The T6 data is again scaled by a factor of 0.45, which corresponds to the ratio of tube diameters in EAST and Oxford. The EAST tests are aligned spatially based on the shock time of arrival sensors to have x=0 at the middle of the integration time. The T6 data was aligned manually to overlap the EAST data. The shift corresponds to 0.8-1.2 cm from their reported zero location. The width of the non-equilibrium peak in EAST is determined primarily by the exposure time of the camera. In the ultraviolet, EAST tests 33 and 39 used exposure times of 1 μs, while tests 41 and 42 used 0.5 and 0.25 μs, respectively. The T6 measurement used an exposure time of 1 μs but has additional broadening due to the optical set up. Non-equilibrium peak height varies inversely with exposure time and peak width, as expected. The region following the non-equilibrium peak is relatively flat and in general agreement between the tests. The EAST results span from 2.1-2.9 W/cm^2-sr, while the T6 data is approximately 3 W/cm^2-sr. The post-shock profile in T6 is relatively flat, as are EAST tests 39 and 41. Besides contamination, reasons for a gradual increase in radiance with distance behind the shock can include deceleration in the tube and flow stagnation at the contact front [42, 43]. In the visible range from 600-850 nm, similar observations can be made. The exposure times in EAST are the same as in the ultraviolet, except for shot 33 which was run at 3 μs. The T6 measurement used 0.5 μs exposure but still has significant optical broadening. The post-shock radiances in EAST vary from 0.4-0.5 W/cm^2-sr while the T6 radiance is near 0.7 W/cm^2-sr. The post-

shock radiance in T6 is again relatively flat, while the EAST tests display a rise of up to 0.1 W/cm^2-sr. Test 39 is relatively flat except for a step change at ~4 cm, which correlates with the appearance of aluminum contamination in the ultraviolet. Spatial profiles in the infrared and near-UV range show similar characteristics in EAST but were not collected in T6, so these measurements are not shown.

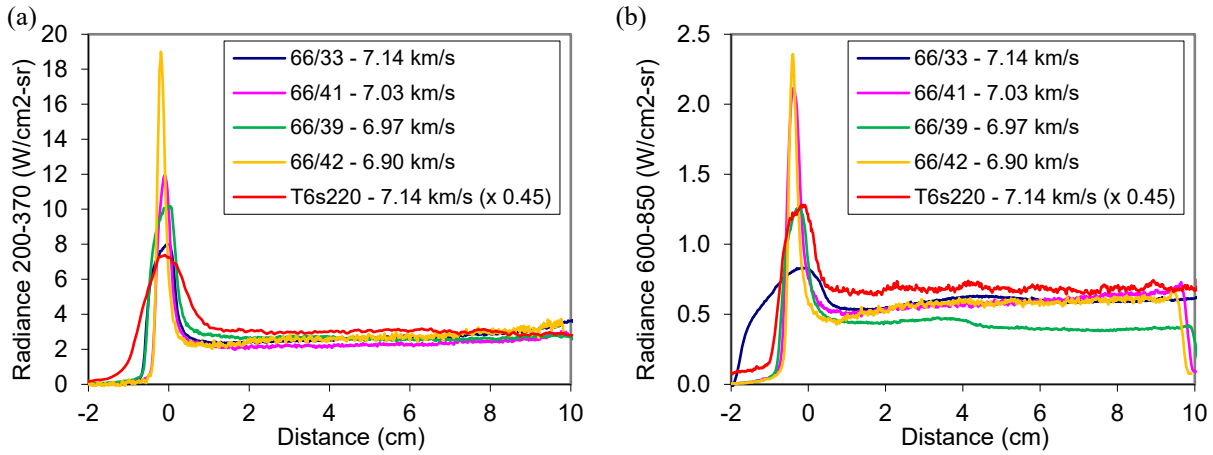

Figure 13. Comparison of radiance behind the shock front at (nominally) 7 km/s and 1.4 Torr.

Spectral comparisons provide additional insight to the data comparisons and are given in Figure 14. In this figure, data from all four cameras (in EAST) are shown and are averaged in the region of x=2 to 4 cm. The EAST data are all within a similar magnitude and are mostly overlapping. The T6 data is also in reasonable agreement with EAST but tends slightly higher. Co-plotted with the data are equilibrium predictions from NEQAIR. Photorecombination increases the NEQAIR prediction slightly in the UV but is insignificant at higher wavelengths and thus not shown. Equilibrium generally tends to underpredict the spectra. Starting from the ultraviolet spectrum, the T6 data tends to agree well with EAST in the middle of the spectrum, but deviates at high and low wavelengths. The equilibrium prediction particularly underpredicts the NO UV radiation, but is lower than the N_2 and N_2^+ molecular features at higher wavelength as well. Introducing about 4 ppm of CN and 40 ppm of OH improves agreement with the features at 390 and 310 nm, respectively. In order to match the spectrum, it would be necessary to increase the NO electronic populations by approximately a factor of 2 and N_2^+ by 1.3. With these adjustments, the N_2 Boltzmann distribution does a reasonably good job of predicting the N_2 2nd positive features at 314 and 336 nm. In the near-UV range (330-490 nm, Figure 14(b)), band radiation is underpredicted, as also seen in the Figure 14(a). Introducing CN impurity and increasing $N_2^+(B^2\Sigma_u^+)$ concentration may improve some of the underprediction, but an offset of about 0.8 W/cm^2-sr-μm is still present. This may be attributed to the background continuum source that has been observed but not conclusively identified in multiple facilities.[6, 26, 44] The visible portion of the spectrum in Figure 14(c) displays a similar offset, though the continuum radiation is reduced at higher wavelengths, similar to what was observed in Sect. III.B. The T6 data is slightly above the EAST data in the lower wavelength region of this spectrum, but shows a greater deviation at high wavelength. EAST shots 41 and 42 used a higher spectral resolution (120 μm slit) compared to shots 33 and 39 (250 μm), which explains differences in the width and height of the atomic lines. Additionally, the O 777 nm line is saturated in Shot 33. The T6 tests used 100 μm slits and have correspondingly narrow atomic line widths and larger peak heights. In the infrared, in spite of the different cameras employed in Shot 33 and Shots 39-42, consistent results are obtained across the four shots. In the infrared, the NEQAIR predictions agree well with some features, but is missing others. This is consistent with Sect. III.D. where some weaker NO bands are not modeled in NEQAIR. Some continuum radiation may also be present, decreasing toward low values at high wavelength. It is noted that the photorecombination continuum was not computed beyond 900 nm in this work, although it is unlikely to be of sufficient magnitude to explain this signal.

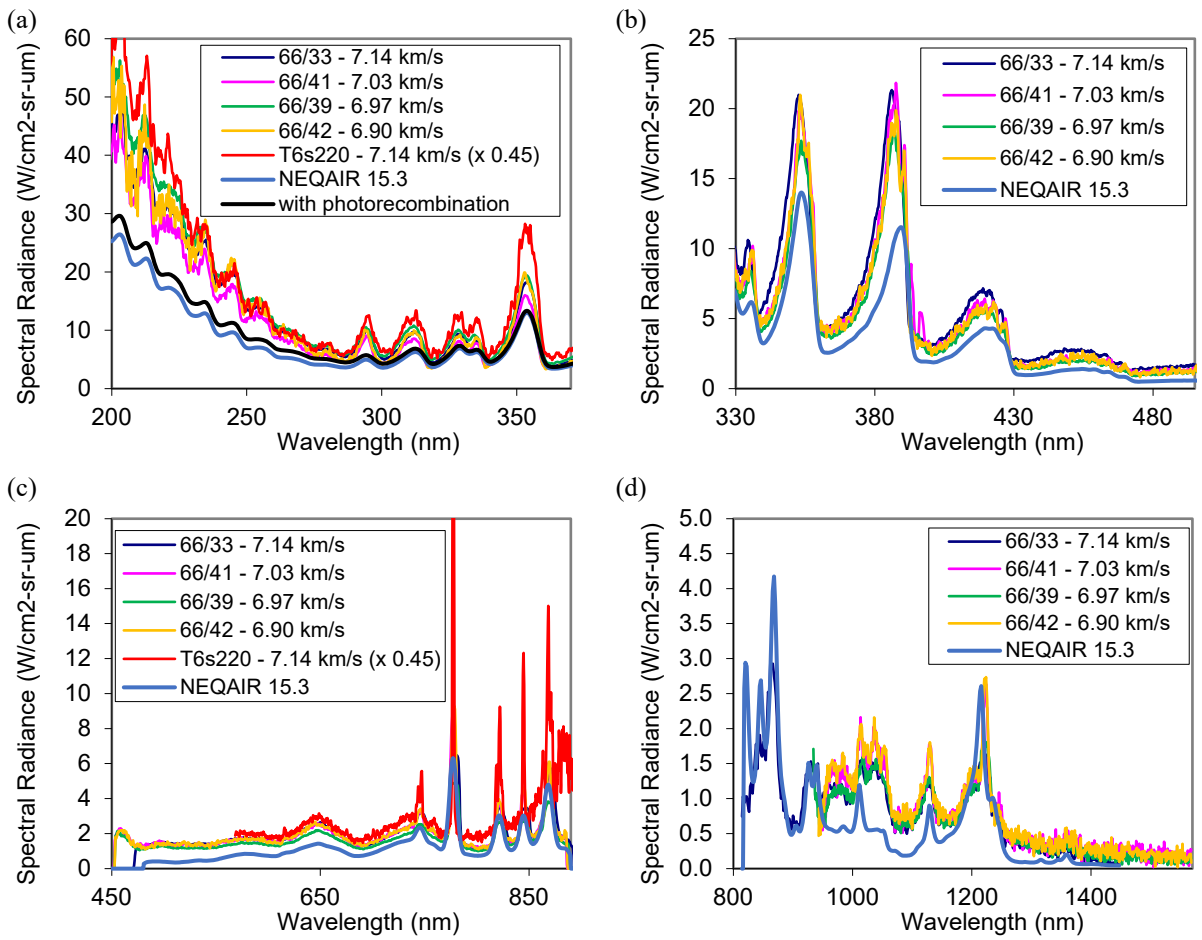

Figure 14. Spectral data behind the shock at 7 km/s and 1.4 Torr obtained in EAST and Oxford T6 facilities. Also shown is the corresponding equilibrium prediction.

F. Comparison to Plasma Torch Data

Measurement of ultraviolet air radiation in an atmospheric plasma torch has been previously reported by Laux, at al., [24] and more recently extended into the vacuum ultraviolet by McGuire, et al. [25]. McGuire's plasma torch experiment shows a relatively flat temperature profile at around 6600K for 2.5 cm before dropping to about 5800K at 4 cm diameter. The spectrum showed good agreement to an equilibrium air model with the SPECAIR code. The plasma torch operates at atmospheric pressure so should be relatively similar to the EAST test conditions at 1 bar. The EAST tests at 6.0 and 7.1 km/s have equilibrium temperatures of 6300 and 6980K so bracket the torch measurement. Figure 15 shows a comparison of the plasma torch data to EAST tests 66/36 and 66/33. The EAST data has been normalized by the tube diameter (10.16 cm) while the plasma torch has been normalized by 4 cm. The plasma torch data has been convolved with the EAST instrument function to obtain an equivalent resolution to the EAST data. Also shown are the equilibrium NEQAIR conditions, including the photorecombination contribution, for each of the experimental conditions. The NEQAIR spectrum agrees with the plasma torch above about 215 nm and has a maximum deviation of 12% at 190 nm. This comparison serves to confirm the accuracy of the NEQAIR prediction. The EAST spectra however are consistently larger than equilibrium, with the data being between 1.5-1.7× higher between 190-260 nm. This corresponds to a similar magnitude of underprediction, starting at 1.9 W/cm^3-sr-μm at 190nm and reducing to 0.3 W/cm^3-sr-μm at 260nm. This difference has dropped below 20%, or 0.1 W/cm^3-sr-μm, by 290 nm.

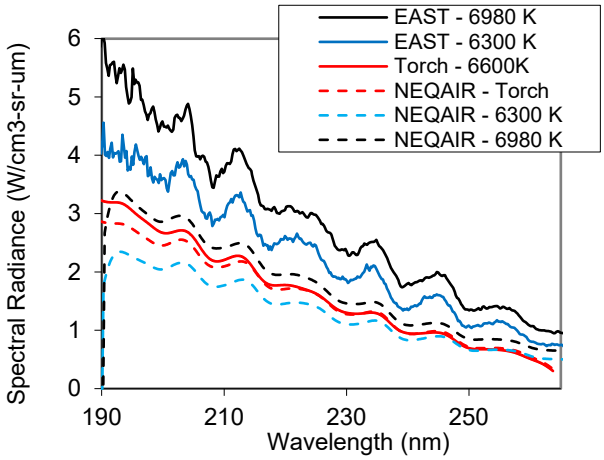

Figure 15. Comparison of EAST data to plasma torch, presented in volumetric units.

IV. Conclusion

This paper describes a low speed air test performed in the NASA Ames EAST facility. Conditions spanned 3-7 km/s at freestream pressures of 1.4-10 Torr. Spectral radiance versus position in the shock is obtained from 200 nm-5.7 μm. Forty-three shots were performed at seven nominal conditions, between 3-5 repeat shots were obtained at each. The paper examined four of these conditions in greater detail, the entire data set will be available on data.nasa.gov. Spectra in the ultraviolet (i.e. <300 nm) showed significant variation in some of the conditions (e.g. at 6 km/s, 2 Torr and 4 km/s, 10 Torr). At other conditions (e.g. 7 km/s, 1.4 Torr) and higher wavelengths, less scatter in the data was observed. Some of the variation may be due to contamination levels, which varied throughout the test series. Readily excited alkali and alkaline metals (Na, K, Ca) were observed at levels on the order of 1-100 ppb, as was aluminum, which is both the tube and primary diaphragm material. These concentrations may influence the ionization levels by several percent but are unlikely to be contributing significant continuum radiation based upon preliminary estimates.

This test is likely the first to measure mid-infrared radiation from the NO molecule in a shock tube. The mid-infrared radiation is fairly weak and subject to low signal-to-noise but was sufficiently strong to compare to predictions with the NEQAIR code. At 10 Torr and 4 km/s, where the post shock pressure is 2.2 bar, the NO infrared radiation is found to be in good agreement with equilibrium. At 2.2 Torr, where the flow is not in equilibrium, the radiation exceeds equilibrium but may be fit to obtain post shock temperatures and NO number density. The vibrational temperature obtained in this way is in good agreement with TDLAS measurements and DSMC model of the flow, however the rotational temperature is lower and the number density is higher. Using the TDLAS data as input to NEQAIR reproduces the (1,0) IR band feature well but does not match the emission profile at higher wavelength. The reason for the mismatch is unclear as TDLAS did probe higher vibrational levels. It may suggest evidence of a non-Boltzmann distribution at high J and v, or could be some undetermined experimental artifact, possibly related to the low signal to noise ratio. The trend of temperature and number density behind the shock is extracted. A peak in vibrational temperature near 7000K is obtained, which may be explained by population of high energy vibrational states through the Zel'dovich reactions. The vibrational temperature relaxes toward the rotational temperature, but remains about 500K below over the measurement range. The rotational temperature on the other hand rises to the post-shock equilibrium temperature. The NO density overshoots equilibrium and is slowly relaxing during the test time.

Measurements in the ultraviolet are well above equilibrium, even when the infrared data appears to be in agreement. Possible omissions from the radiation model were examined and a few were identified. The presence of photorecombination of O_2 (i.e. Schumann-Runge continuum) was shown to raise the radiation in the ultraviolet by as much as 50%. The photorecombination extends out into the visible and had as much as an order of magnitude impact on the weak radiation predicted there. The current estimate of photorecombination however is still below the experimental measurement, except from 280-400 nm. It is suggested that the cross-section calculation can be improved, although other contributors may remain to be identified. Since photorecombination scales as n_O^2, and also inversely with equilibrium constant, it becomes less significant at lower pressure or higher temperature conditions. At the high pressure, low temperature condition where NO radiation is optically thick, the UV radiation is also

sensitive to molecular linewidth and spin splitting, which is not enabled by default in NEQAIR. Updates were made to these contributions and shown to increase the UV radiation by as much as 26%, but having no impact in the visible. Still, with these contributions included, the NO peaks features remain underpredicted, suggesting the NO(A) state is overpopulated by about a factor of 2. This level of overpopulation is observed both in the 2.2 bar and 1 bar post-shock conditions. Comparison to plasma torch data at 6600K and 1 bar suggests it is not a modeling error. Additionally, the NO(C) and O_2(B) states appear depopulated, which may be expected due to pre-dissociation. For the reacting flow condition at 3.8 km/s, this population is used to extract an electronic temperature behind the shock, which is found to be in good agreement with the vibrational temperature.

Measurements made at 1 bar were compared to similar tests collected in the Oxford T6 facility. Overall, the data in EAST and Oxford are in agreement, showing a level of radiation that exceeds equilibrium predictions and similar measurements made in the atmospheric plasma torch facility. The T6 data tends to be somewhat higher than the EAST data, particularly at the edges of the wavelength ranges measured. The data suggests an overpopulation of both NO and N_2^+. N_2 radiation levels appear in rough agreement with Boltzmann populations at equilibrium. The underlying background continuum remains underpredicted. While the continuum may be approximated with a constant shift in the UV/Vis range, in the Vis/NIR it is trending downward at increasing wavelength, similar to the photorecombination continuum. The summary of data then provides confirmation of several aspects of air radiation modeling, but other areas where modeling refinements, including how the experiment itself is modeled, may be possible.

Acknowledgments

Support from the Entry Systems Modeling Project is acknowledged. Brett Cruden is supported through contract NNA15BB15C to AMA, Inc. The authors would like to thank Efaine Chang and Jesse Streicher from the Hanson group at Stanford University for providing the TDLAS data and their model of the O_2 Schumann-Runge continuum for purposes of comparison. Andrea Fagnani (NASA post-doctoral program) is acknowledged for contribution in the latter part of the test series.

References

[1] Brandis, A.M., B.A. Cruden, D. Prabhu, D. Bose, M. McGilvray, R.G. Morgan, *Analysis of Air Radiation Measurements Obtained in the EAST and X2 Shocktube Facilities*, 10th AIAA/ASME Joint Thermophysics and Heat Transfer Conference. (2010)
[2] Brandis, A.M., C.O. Johnston, B.A. Cruden *Investigation of Non-equilibrium Radiation for Earth Entry*, AIAA Thermophysics Conference. (2016)
[3] Brandis, A.M., C.O. Johnston, B.A. Cruden, D.K. Prabhu, J. Thermophys. Heat Transf. **31**, 178-192 (2017)
[4] Cruden, B.A., J. Thermophys. Heat Transf. **26**, 222-230 (2012)
[5] Cruden, B.A., A.M. Brandis, J. Thermophys. Heat Transf. **34**, 154-180 (2020)
[6] Cruden, B.A., R. Martinez, J.H. Grinstead, J. Olejniczak, *Simultaneous Vacuum Ultraviolet through Near IR Absolute Radiation Measurement with Spatiotemporal Resolution in an Electric Arc Shock Tube*, 41st AIAA Thermophysics Conference. (2009)
[7] Tibère-Inglesse, A.C., K. Bensassi, A.M. Brandis, B.A. Cruden, *Shock tube radiation measurement in expanding air flows*, AIAA SCITECH 2022 Forum. (2022)
[8] Brandis, A., C. Johnston, B. Cruden, D. Prabhu, D. Bose, *Validation of High Speed Earth Atmospheric Entry Radiative Heating from 9.5 to 15.5 km/s*, 43rd AIAA Thermophysics Conference. (2012)
[9] Tibère-Inglesse, A., B.A. Cruden, Journal of Quantitative Spectroscopy and Radiative Transfer **290**, (2022)
[10] Brandis, A.M., B.A. Cruden *Shock Tube Radiation Measurements in Nitrogen*, (2018)
[11] Adhikari, N., A. Alexeenko, *An Assessment of Two-Temperature Dissociation Models for Vibrational Nonequilibrium Flows*, AIAA AVIATION 2023 Forum. (2023)
[12] Torres, E., T. Gross, T.E. Schwartzentruber, *Implementation of new multi-temperature nonequilibrium air chemistry model for CFD based on first-principles calculations*, AIAA AVIATION 2023 Forum. (2023)
[13] Chaudhry, R.S., I.D. Boyd, *Parametric Comparison of the Park and MMT Chemical Kinetics Models with Multiple Freestream Speeds*, AIAA AVIATION 2023 Forum. (2023)
[14] Aiken, T.T., I.D. Boyd, *Analysis of Critical Rate Processes for Ionization in Shock-Heated Air*, AIAA AVIATION 2023 Forum. (2023)
[15] E. Chang, J.W.S., C. L. Strand, R. K. Hanson, A. C. Tibere-Inglesse, B. A. Cruden, *Rapid-Scanning Tunable Laser Absorption Measurements of Shock-Heated Nonequilibrium Air Species in the NASA Electric Arc Shock Tube*, International Symposium on Shock Waves. (2023)

[16] Yanes, N.J., J.M. Austin, *Nitric Oxide Spectroscopic Measurements in a Hypervelocity Stagnation Flow*, AIAA Scitech 2019 Forum. (2019)
[17] Karpuzcu, I.T., M.P. Jouffray, D.A. Levin, J. Thermophys. Heat Transf. **36**, 982-1002 (2022)
[18] Daniel, K., E. Jans, K.P. Lynch, W. Swain, C. Downing, J.L. Wagner, *Nitric Oxide Emission Spectroscopy of a Cylinder Stagnation Flow in a Shock Tunnel*, AIAA SCITECH 2023 Forum. (2023)
[19] Karpuzcu, I.T., S. Thirani, D.A. Levin, D. Andrienko, *Nitric Oxide Infrared Radiation Modeling from a Hypersonic Flow*, AIAA AVIATION 2022 Forum. (2022)
[20] Cruden, B.A., A.M. Brandis, M.E. MacDonald, *Characterization of CO Thermochemistry in Incident Shockwaves*, 2018 Joint Thermophysics and Heat Transfer Conference. (2018)
[21] Cruden, B.A., A.M. Brandis, D.K. Prabhu, *Measurement and Characterization of Mid-wave Infrared Radiation in CO_2 Shocks*, 11th AIAA/ASME Joint Thermophysics and Heat Transfer Conference. (2014)
[22] Thirani, S., I.T. Karpuzcu, D.A. Levin, *Modeling of Unsteady 1D Shocks Using the DSMC Approach to Estimate Emission Spectra*, AIAA AVIATION 2023 Forum. (2023)
[23] Laux, C.O., *Optical diagnostics and radiative emission of air plasmas*, (1993)
[24] Laux, C.O., T.G. Spence, C.H. Kruger, R.N. Zare, Plasma Sources Science and Technology **12**, 125-138 (2003)
[25] McGuire, S.D., C. Jacobs, P.B. Mariotto, C.H.C. Grimaldi, A. Tibère-Inglesse, C.O. Laux, J. Thermophys. Heat Transf. **37**, 821-832 (2023)
[26] Glenn, A.B., P.L. Collen, M. McGilvray, *Experimental Non-Equilibrium Radiation Measurements for Low-Earth Orbit Return*, AIAA SCITECH 2022 Forum. (2022)
[27] Cruden , B.A., *Absolute Radiation Measurements in Earth and Mars Entry Conditions*, (2014)
[28] Aaron M. Brandis, B.A.C., *NEQAIR v15.0 Release Notes: Nonequilibrium and Equilibrium Radiative Transport and Spectra Program*, (2019)
[29] McBride, B.J., S. Gordon, *Computer program for calculation of complex chemical equilibrium compositions and applications II. User's Manual and Program Description*, (1996)
[30] Cunto, W., C. Mendoza, F. Ochsenbein, C. Zeippen, The Opacity Project: Selected research papers-Atomic Data Tables for S to Fe **2**, 53 (1994)
[31] Krish, A., J.W. Streicher, R.K. Hanson, Journal of Quantitative Spectroscopy and Radiative Transfer **247**, (2020)
[32] Bykova, N.G., L.A. Kuznetsova, Optics and Spectroscopy **105**, 668-673 (2008)
[33] Gibson, S., *PyDiatomic: PyDiatomic initial release (v0.1-alpha)*, (2016)
[34] Lewis, B.R., S.T. Gibson, F.T. Hawes, L.W. Torop, Phys. Chem. Earth (C) **26**, 519-526 (2001)
[35] Lewis, B.R., S.T. Gibson, P.M. Dooley, The Journal of Chemical Physics **100**, 7012-7035 (1994)
[36] NICOLET, M., S. CIESLlK, R. KENNES, Planet. Space Sci. **37**, 427-458 (1989)
[37] Cheung, A.S.-C., K. Yoshino, J.R. Esmond, W.H. Parkinson, JOURNAL OF MOLECULAR SPECTROSCOPY **178**, 66–77 (1996)
[38] Griem, H.R., *Spectral Line Broadening by Plasmas*, (Acad Press, New York),
[39] Child, M.S., J. Phys. B: Atom. Mol. Phys **13**, 2557 (1980)
[40] Bose, D., G.V. Candler, J. Thermophys. Heat Transf. **12**, 214-222 (1998)
[41] Laux, C.O., R.J. Gessman, B. Hilbert, C.H. Kruger, *EXPERIMENTAL STUDY AND MODELING OF INFRARED AIR PLASMA RADIATION*, AIAA 95-2124 (1995)
[42] Collen, P.L., M. Satchell, L. di Mare, M. McGilvray, *Analysis of Shock Deceleration Effects on Radiation Experiments in the NASA Electric Arc Shock Tube*, AIAA SCITECH 2022 Forum. (2022)
[43] Clarke, J., L. Di Mare, M. McGilvray, AIAA J. **61**, 3365-3374 (2023)
[44] Johnston, C.O., B.R. Hollis, K. Sutton, Journal of Spacecraft and Rockets **45**, 865-878 (2008)